

Dispersive spherical optical model of neutron scattering from ^{27}Al up to 250 MeV

A. Molina^{*1}, R. Capote^{†1,2}, J. M. Quesada^{‡1} and M. Lozano^{§1}

¹*Departamento de Física Atómica, Molecular y Nuclear,*

Universidad de Sevilla, Facultad de Física, AP 1065, E-41080 Sevilla, Spain

²*Centro de Estudios Aplicados al Desarrollo Nuclear, AP 100, Miramar, La Habana, Cuba*

(October 24, 2018)

A spherical optical model potential (OMP) containing a dispersive term is used to fit the available experimental database of $\sigma(\theta)$ and σ_T for n+ ^{27}Al covering the energy range 0.1- 250 MeV using relativistic kinematics and a relativistic extension of the Schroedinger equation. A dispersive OMP with parameters that show a smooth energy dependence and energy independent geometry are determined from fits to the entire data set. A very good overall agreement between experimental data and predictions is achieved up to 150 MeV. Inclusion of nonlocality effects in the absorptive volume potential allows to achieve an excellent agreement up to 250 MeV.

PACS number(s): 11.55.Fv, 24.10.Ht, 02.60.Jh

I. INTRODUCTION

During the last fifteen years, a great deal of theoretical attention has been devoted to casting a proper formulation of the nuclear mean field at positive and negative energies. A significant contribution to the solution of this problem can be considered the work of Mahaux and co-workers on dispersive optical-model analysis [1–5]. The unified description of nuclear mean field in dispersive optical-model is accomplished by using a dispersion relation, which links the real and absorptive terms of the optical model potential. The dispersive optical model (DOM) provides a natural extension of the optical model derived data into the bound state region. In this way a physically self-consistent description of the energy dependence of the OMP is obtained and the prediction of single-particle, bound state quantities using the same potential at negative energies became possible. Moreover additional constraint imposed by dispersion relations helps to reduce the ambiguities in deriving phenomenological OMP parameters from the experimental data.

Dispersive OMP analysis has been applied to nucleus-nucleus systems [6–9], where the energy dependence of the real central potential at low energies near the Coulomb barrier has been studied, and contributions of the dispersion terms are evaluated. However for a nucleus-nucleus system, the dispersive OMP analysis is limited to the positive energy region, because it is not yet clear how to deal with particle clusters bound in a nucleus. Some progress have been achieved in applications of the dispersive OMP analysis to the alpha-nucleus scattering, improving our knowledge of the alpha cluster effective interaction inside nuclear system [10]. On the other hand a great success has been achieved in deriving DOM potentials for nucleon scattering on closed shell nuclei like ^{40}Ca [4,11–14], ^{90}Zr [14–18] and ^{208}Pb [1–4,11,12,19,20], for which experimental information on bound-states is available. Many studies have dealt also with neutron scattering on non magic nuclei (^{39}K [21], ^{51}V [22], ^{86}Kr [23], ^{89}Y [24], ^{93}Nb [25], ^{113}In [26] and ^{209}Bi [20,27,28]). However very few studies have been devoted to DOM potentials for nuclei with $A \lesssim 30$. Only one preliminary DOM analysis has been reported for $^{27}\text{Al}(n, n)$ [29]. There are two publications making a DOM analysis for proton induced reactions on aluminium up to 60 MeV [30,31].

The main purpose of this contribution is to construct a complex mean field felt by neutrons in ^{27}Al theoretically valid from -50 up to 250 MeV energy. There exist two main versions of the dispersion relation approach. In both methods, the real and imaginary parts of the mean field are connected by a dispersion relation and, moreover, the mean field is required to closely reproduce the experimental value of the Fermi energy E_F . The main difference between the two methods is the following: (i) In the "variational moment approach" [11,12], the parameters of the complex mean field are determined by fitting radial moments of phenomenological optical-model potentials. (ii) In the "dispersive optical model analysis" [13–15], the unknown parameters are derived by performing optical-model fits to experimental scattering cross sections that need to be available over an energy range as broad as possible.

*e-mail: alberto@nucle.us.es

†e-mail: rcapotenoy@yahoo.com

‡e-mail: quesada@cica.es

§e-mail: lozano@cica.es

In the present work a variation of the dispersive optical model analysis is applied to the determination of the nuclear mean field for the neutron- ^{27}Al system. An Ohio University - Los Alamos collaboration has published an extensive survey of neutron-nucleus total cross section measurements up to 600 MeV [32,33]. These high precision data together with earlier neutron differential scattering data available in the interval 1-26 MeV form the database considered at positive energies. Fermi energy value derived from nuclear masses is used to constrain the mean field value at negative energies. Therefore the energy variation of the model parameters is reasonably defined over a wide range, an extremely important point for a successful dispersive analysis. Remarkable is the fact that our total cross section database goes up to the region where surface absorption can be safely neglected. Since the employed database extends up to 250 MeV and since the recent σ_T data are very accurate, i.e. the uncertainty $\Delta\sigma_T$ is about $\pm 1\%$, we use relativistic kinematics and a relativistic equivalent to the Schroedinger equation in all our calculations.

Other motivation for our work is that aluminium is an important structural material for the accelerator-driven systems and its cross sections are often used as references to determine other cross sections [34]. There exist phenomenological OMP (in the sense that dispersive relations constrain is not used) describing neutron scattering on aluminium up to high incident energy. The LANL high energy evaluation of Chadwick *et al* [35] employed the OMP of Petler *et al* [36] up to 60 MeV and the Madland global OMP [37] from 60 up to 150 MeV. Lee and coworkers [38] derived a new phenomenological OMP which described neutron scattering from ^{27}Al up to 250 MeV incident energy. Recently a new global phenomenological parametrization valid from 1 keV to 200 MeV for $A \geq 27$ nuclei was proposed by Koning and Delaroche [39].

Usually in DOM analysis the absorptive potentials are considered symmetric about the Fermi energy E_F and non-zero in the energy gap surrounding E_F . However in the contribution from Mahaux and Sartor [4] they pointed out that (i) due to nonlocality effects, the absorptive potential will be highly asymmetric (with respect to E_F) and (ii) there should be an energy gap centered about E_F in which the absorption term drops to zero, at least for energies between the first-hole and first-particle state. Recent DOM analysis of neutron scattering on ^{208}Pb and ^{209}Bi [20] failed to describe σ_T data for energies above 40 MeV using asymmetric version of the absorptive potentials for large positive and large negative energies. We will present strong evidence to favour asymmetric absorptive potentials for proper description of the neutron scattering σ_T data for energies between 150 and 250 MeV.

The paper is structured as follows. Section II provides a description of the dispersive optical model formalism, the solved wave equation and the forms of the energy and radial dependencies of the real, imaginary and spin-orbit potentials. Section III describes the compound nucleus (CN) calculations, the $^{27}\text{Al}(n,n)$ experimental database, our procedure for searching, and the resulting relativistic and non-relativistic spherical DOM potentials for $^{27}\text{Al}(n,n)$. In the same section we compare derived DOM potentials with phenomenological potentials and experimental data. Finally Section IV contains our conclusions.

II. DOM FORMALISM

A. Optical-model potential and wave equation

The optical-model analysis was carried out with a semirelativistic generalization of the conventional nonrelativistic Schroedinger formulation of the scattering process [40]. Relativistic kinematics was used for the projectile, but it was assumed that the target motion in the center-of-mass system could be treated nonrelativistically. A relativistic equivalent to the Schroedinger equation was generated by appropriate reduction of the Dirac equation for a massive, energetic fermion (mass m and c.m. wave number k) moving in a localized central potential $V(r)$ taken as the time-like component of a Lorentz four-vector. In the reduced two-body problem with relativistic projectile but nonrelativistic target (mass M) the large component of the partial wave function $F_l(\rho)$ can be shown to satisfy the radial equation

$$\left\{ \frac{d^2}{d\rho^2} + \left[1 - \frac{V(\rho)}{T_c} - \frac{l(l+1)}{\rho^2} \right] \right\} F_l(\rho) = 0 \quad (1)$$

where $\rho = kr$, T_c is the total c.m. kinetic energy, l is the orbital angular momentum, and $V(\rho)$ is the renormalized nuclear optical potential

$$V(\rho) = \gamma U(r), \gamma = 1 + \frac{T_c}{T_c + 2m} \quad (2)$$

Equation (1) is formally identical to the radial equation for the solution of the non-relativistic Schroedinger equation for the analogous scattering problem with a nuclear potential renormalized by a factor γ . This factor becomes increasingly important as the projectile kinetic energy increases (see equation (2)) leading to an effective increase of

the potential depth. The spin-orbit term in $V(r)$ employed in this analysis is a purely phenomenological one since the intrinsic SO term in the Dirac equation is negligible small in the above limits. Equation (1) was used in all calculations. In a non-relativistic case we set a factor γ equal to 1 and non-relativistic kinematics was employed, otherwise relativistic kinematics and the factor γ according to equation (2) were used.

Our analysis spans an energy range from 0.1 up to 250 MeV. Both direct and statistical processes contribute to nucleon-nucleus elastic scattering at these energies. According to our estimation the statistical processes are important up to 12 MeV in aluminium. Compound nucleus calculation will be described in the next section. The direct processes, increasingly dominant at higher energies, can be described by the optical model. Although ^{27}Al nucleus is deformed, the spherical OMP has been applied successfully [36,38,41]. *A posteriori* analysis of the impact of this approximation on the calculated observables will be discussed below.

The optical model potential may be written as

$$\begin{aligned}
U(r, E) = & - [V_v(E) + iW_v(r, E)] f_{WS}(r, R_v, a_v) \\
& - [V_s(E) + iW_s(r, E)] g_{WS}(r, R_s, a_s) \\
& - \left(\frac{\hbar}{m_\pi c} \right)^2 [V_{so}(E) + iW_{so}(E)] \times \frac{1}{r} g_{WS}(r, R_{so}, a_{so}) (\vec{l} \cdot \vec{\sigma})
\end{aligned} \tag{3}$$

where the successive complex-valued terms are the volume central, surface central and spin-orbit potentials. The volume shape $f_{WS}(r, R_v, a_v)$ is a standard Woods-Saxon form factor specified by a potential radius R_v and diffuseness a_v . The surface(spun-orbit) shape is the first derivative of the Woods-Saxon form specified by a potential radius $R_s(R_{so})$ and diffuseness $a_s(a_{so})$

$$g_{WS}(r, R_i, a_i) = -4a_i \frac{d}{dr} f(r, R_i, a_i) \tag{4}$$

The reduced radius parameter r_i is introduced as usual by the relation $R_i = r_i A^{1/3}$. In our formulation of the OMP in Eq.(3) the real and imaginary central volume terms share the same geometry parameters r_v and a_v and likewise the real and imaginary central surface terms share the same r_s and a_s . This assumption [3] can be seen as a consequence of the dispersive relations, allowing us to reduce the number of geometrical parameters in the OMP.

For the spin-orbit potential we adopt the parameters obtained by Koning *et al* [34], namely:

$$\begin{aligned}
V_{so}(E) &= 6.0 \exp(-0.005E) \text{ MeV} \\
W_{so}(E) &= 0.2 - 0.011E \text{ MeV} \\
r_{so} &= 1.017 \text{ fm}, \quad a_{so} = 0.6 \text{ fm}
\end{aligned} \tag{5}$$

In a dispersion relation treatment, the real central potential strength consists of a term which varies slowly with energy, the so called Hartree-Fock (HF) term, $V_{HF}(E)$, plus a correction term, $\Delta V(E)$, which is calculated using a dispersion relation. The depth of the dispersive term of the potential $\Delta V(E)$ can be written in the subtracted form

$$\Delta V(E) = \frac{\mathcal{P}}{\pi} \int_{-\infty}^{\infty} W(E') \left(\frac{1}{E' - E} - \frac{1}{E' - E_F} \right) dE' \tag{6}$$

With the assumption that $W(E)$ be symmetric respect to the Fermi energy E_F , Eq.(6) can be expressed in a form which is stable under numerical treatment [15], namely:

$$\Delta V(E) = \frac{2}{\pi} (E - E_F) \int_{E_F}^{\infty} \frac{W(E') - W(E)}{(E' - E_F)^2 - (E - E_F)^2} dE' \tag{7}$$

where $W(E)$ is the imaginary part of the OMP. The dispersive term $\Delta V(E)$ is divided into two terms $\Delta V_v(E)$ and $\Delta V_s(E)$, which arise through dispersion relations (7) from the volume $W_v(E)$ and surface $W_s(E)$ imaginary potentials respectively. If imaginary potential geometry is energy dependent, then radial dependence of the dispersive correction can not be expressed using a Wood-Saxon form factor, i.e $\Delta V_v(r, E) \neq \Delta V(E) f(r, R, a)$. However, to simplify the problem, the OMP geometry parameters used in this work are energy independent. In this case, using the definitions of the equation (3), the real volume $V_v(E)$ and surface $V_s(E)$ central part of the DOM potential are given by

$$\begin{aligned}
V_v(E) &= V_{HF}(E) + \Delta V_v(E) \\
V_s(E) &= \Delta V_s(E)
\end{aligned} \tag{8}$$

It is known that the energy dependence of the depth $V_{HF}(E)$ is due to the replacement of a microscopic nonlocal HF potential by a local equivalent. For a gaussian non-locality $V_{HF}(E)$ is a linear function of E for large negative E and is an exponential for large positive E . Following Mahaux and Sartor [4], the energy dependence of the Hartree-Fock part of the nuclear mean field is taken as that found by Lipperheide [42]:

$$V_{HF}(E) = V_0 \exp(-\alpha_{HF}(E - E_F)) \quad (9)$$

where the parameters V_0 and α_{HF} are undetermined constants. This equation (9) can be used to describe HF potential in the scattering regime [4].

It is useful to represent the variation of surface $W_s(E)$ and volume absorption potential $W_v(E)$ depth with energy in functional forms suitable for the dispersive optical model analysis. An energy dependence for the imaginary volume term has been suggested in studies of nuclear matter theory [43]:

$$W_v(E) = A_v \frac{(E - E_F)^n}{(E - E_F)^n + (B_v)^n} \quad (10)$$

where A_v and B_v are undetermined constants. Following Mahaux and Sartor [2] we adopt $n = 4$. An energy dependence for the imaginary-surface term has been suggested by Delaroche *et al* [15] to be:

$$W_s(E) = A_s \frac{(E - E_F)^m}{(E - E_F)^m + (B_s)^m} \exp(-C_s|E - E_F|) \quad (11)$$

where $m = 4$ and A_s, B_s and C_s are undetermined constants.

According to equations (10) and (11) the imaginary part of the OMP is assumed to be zero at $E = E_F$ and nonzero everywhere else. A more realistic parametrization of $W_v(E)$ and $W_s(E)$ forces these terms to be zero in some region around the Fermi energy. A physically reasonable energy for defining such a region is the average energy of the single-particle states E_P [4]. For aluminium we used a value $E_P = -5.66$ MeV, obtained by averaging the first three particle states reported in the microscopical single-particle level calculation by Moller and Nix [44]. The experimental value of the Fermi energy E_F derived from mass differences is equal to -10.392 MeV.

Therefore a new definition for imaginary part of the OMP can be written as:

$$W_v(E) = \begin{cases} 0 & \text{for } E_F < E < E_P \\ A_v \frac{(E - E_P)^n}{(E - E_P)^n + (B_v)^n} & \text{for } E_P < E \end{cases} \quad (12)$$

and likewise for surface absorption.

$$W_s(E) = \begin{cases} 0 & \text{for } E_F < E < E_P \\ A_s \frac{(E - E_P)^m}{(E - E_P)^m + (B_s)^m} \exp(-C_s|E - E_P|) & \text{for } E_P < E \end{cases} \quad (13)$$

The symmetry condition

$$W(2E_F - E) = W(E) \quad (14)$$

is used to define imaginary part of the OMP for energies below the Fermi energy. Equations (12) and (13) are used to describe imaginary absorptive potential in this contribution.

B. High energy behavior of the volume absorption

The assumption that imaginary potential $W_v(E)$ is symmetric about $E' = E_F$ (according to equation (14)) is plausible for small values of $|E' - E_F|$, however as was pointed out by Mahaux and Sartor [4] this approximate symmetry no longer holds for large values of $|E' - E_F|$. In fact the influence of the nonlocality of the imaginary part

of the microscopic mean field will produce an increase of the empirical imaginary part $W(r, E')$ at large positive E' and approaches zero at large negative E' [1,45]. Following Mahaux and Sartor [4], we assume that the absorption strengths are not modified below some fixed energy E_a . They used $E_a = 60$ MeV, however this value is fairly arbitrary [4]. Let assume the non-local imaginary potential to be used in the dispersive integral is denoted by $\widetilde{W}_v(E)$, then we can write [5]

$$\widetilde{W}_v(E) = W_v(E) \left[1 - \frac{(E_F - E - E_a)^2}{(E_F - E - E_a)^2 + E_a^2} \right], \text{ for } E < E_F - E_a \quad (15)$$

and

$$\widetilde{W}_v(E) = W_v(E) + \alpha \left[\sqrt{E} + \frac{(E_F + E_a)^{3/2}}{2E} - \frac{3}{2} \sqrt{(E_F + E_a)} \right], \text{ for } E > E_F + E_a \quad (16)$$

These functional forms are chosen in such a way that the function and its first derivative are continuous at $E' = |E_F - E_a|$. At large positive energies nucleons sense the "hard core" repulsive region of the nucleon-nucleon interaction and $\widetilde{W}_v(E)$ diverges like $\alpha\sqrt{E}$. Using a model of a dilute Fermi gas hard-sphere the coefficient α can be estimated to be equal to $1.65 \text{ MeV}^{1/2}$ [45], assuming that the Fermi impulse k_F is equal to 1.36 fm^{-1} and the radius of the repulsive hard core is equal to 0.4 fm . On the contrary, at large negative energies the volume absorption decreases and goes asymptotically to zero. The non-local imaginary absorption potential $\widetilde{W}_v(E)$ and the symmetric imaginary absorption potential $W(E)$ are represented by solid and dotted lines respectively in the lower panel of figure 1.

The asymmetric form of the volume imaginary potential of equations (15) and (16) results in a dispersion relation that must be calculated directly from Eq.(6) and separates into three additive terms [46]. Therefore, we write the dispersive correction in the form

$$\Delta\widetilde{V}_v(E) = \Delta V_v(E) + \Delta V_{<}(E) + \Delta V_{>}(E) \quad (17)$$

where $\Delta V_v(E)$ is the dispersive correction due to the symmetric imaginary potential of equation (12) and the terms $\Delta V_{<}(E)$ and $\Delta V_{>}(E)$ are the dispersive corrections due to the asymmetric terms of equations (15) and (16), respectively. The resulting energy dependence of the dispersive integrals $\Delta\widetilde{V}_v(E)$ and $\Delta V_v(E)$ for both non-local imaginary absorption potential $\widetilde{W}_v(E)$ and symmetric imaginary absorption potential $W(E)$ is represented by solid and dotted lines respectively in the upper panel of figure 1. While the symmetric case features an equal contribution coming from negative and positive energies, in the asymmetric case the negative energy contribution to the dispersive integral is very different to the positive energy value. The resulting dispersive correction for the asymmetric case starts to increase already for energies above 50 MeV , making a significant contribution to the real part of the OMP.

It should be noted that non-locality corrections (equations (15) and (16)) can be used either for volume or surface imaginary potential; however, Mahaux and Sartor [4] have shown that nonlocality consideration for the surface imaginary potential has a very small effect on calculated cross sections. Therefore in this work we followed Ref. [5] and only considered the effects of nonlocality in the volume absorption.

III. DISPERSIVE OPTICAL MODEL ANALYSIS

A. DOM software

Search optical model codes ECIS95 in the external input mode [47,48] and COH v 2.2 [49] were used for DOM analyses using relativistic and non-relativistic kinematics respectively. A modification was introduced into the later code to force equality of the real and imaginary surface(volume) geometry parameters $R_s, a_s(R_v, a_v)$ during the search procedure, as it is implicit in the equation (3). The code does not include the dispersion relations, therefore the dispersion integrals (7) of the symmetric forms (12) and (13) of the imaginary potential were calculated numerically using a Gauss quadrature method [50], while the asymmetric contribution was calculated analytically (see Eqs.(16-19) of Ref. [46]). An auxiliary code system was developed to produce proper input data sets for both optical model codes and to calculate for each data set(i.e. for each energy) the χ^2 quantity according to:

$$\chi^2(E) = \sum_{i=1}^{N_\sigma} \left[\frac{\sigma_{\text{exp}}(E, \theta_i) - \sigma_{\text{calc}}(E, \theta_i)}{\Delta\sigma_{\text{exp}}(E, \theta_i)} \right]^2 + \left[\frac{\sigma_{\text{exp}}^{\text{tot}}(E) - \sigma_{\text{calc}}^{\text{tot}}(E)}{\Delta\sigma_{\text{exp}}^{\text{tot}}(E)} \right]^2 \quad (18)$$

Here, $\sigma_{calc}(E, \theta_i)[\sigma_{calc}^{tot}(E)]$ and $\sigma_{exp}(E, \theta_i)[\sigma_{exp}^{tot}(E)]$, are the differential(total) cross sections from the optical model calculations and experiments for a given laboratory energy E , respectively, and $\Delta\sigma_{exp}(E, \theta_i)[\Delta\sigma_{exp}^{tot}(E)]$ is the experimental uncertainty reported. The N_σ is the number of data points for $\sigma_{exp}(E, \theta_i)$. Our code system allows to finetune the OMP parameters of interest to minimize the total search χ^2 of the entire data set.

B. Summary of the experimental databases

A survey of the experimental data spanning from 0.1 to 250 MeV used in the DOM analyses is presented in this section. The $^{27}\text{Al}(n,n)\sigma(\theta)$ data were obtained from Towle and Gilboy [51] at 1, 2.3 and 4 MeV; Tanaka *et al* [52] at 4.8, 6.7 and 8 MeV; Kinney and Perey [53] at 5.4, 6.4, 7.5 and 8.6 MeV; Dagge *et al* [54] at 7.62 MeV; Velkley *et al* [55] at 9 MeV; Boerker *et al* [56] at 10.2 MeV; Whisnant *et al* [41] at 11, 14 and 17 MeV; Petler *et al* [36] at 18, 20, 22, 25 and 26 MeV; Bratenahl *et al* [57] at 84 MeV; Salmon [58] at 96 MeV and Van Zyl *et al* [59] at 136 MeV. The $^{27}\text{Al}(n,n)A_y(\theta)$ data were obtained from Dagge *et al* [54] at 7.62 MeV and Martin and Walter [60] at 14 and 17 MeV. These polarization data were used only for testing spin-orbit interaction. Energy-averaged total cross sections σ_T for ^{27}Al were obtained from Finlay *et al* [32, 33] from 5.3 to 250 MeV. Additional energy-averaged σ_T data were taken from Refs. [61–72] to be used for comparing predictions of the model. We selected measurements containing several points in energy, specially all with data above 20 MeV. In critiquing all the available experimental total cross section data, the high resolution cross section data of Ref. [73] was found to be inconsistent with the rest of the data set and was ignored in our analysis.

C. Compound-nucleus corrections

The statistical model of nuclear reaction according to the Hauser-Feshbach theory [74] with width fluctuation corrections as modified by Moldauer [75] is used to compute the CN contributions to the elastic channel. When the cross section is averaged over many CN resonances the shape elastic differential cross section can be incoherently added to the compound elastic contribution to compare with the experimentally observed elastic-scattering cross section. For neutron energies larger than 12 MeV, the compound-elastic contribution can be neglected. The CN cross section calculation is built-in inside the search code CoH [49]. Three reaction channels are considered in the statistical-model calculations of the ^{28}Al CN decay: (n,n), (n,p) and (n, α). Transmission coefficients for proton and alpha emission in the exit channels are calculated from the spherical OMP parameters by Perey *et al* [76] and Arthur and Young [77] (a modification of Lemos OMP [78]) respectively. The transmission coefficients in the entrance and inelastic channel were calculated using the DOM potential of the present work.

Discrete level information is used to represent the low-lying states and the Gilbert-Cameron level density formulae [79] are used to represent the high-lying continuum of states. Figure 2 shows the cumulative number of levels as a function of excitation energy for the residual nuclei of the three reaction channels. The discrete state data are taken from the Belgia compilation contained in RIPL [44]. The vertical lines indicate the cut-off energy between the discrete states and the continuum. It is well known that a CN calculation is highly sensitive to the level density parameters modeling the continuum of the excited states. We used the "constant temperature" formula [79] to estimate the total number of excited states available at excitation energy E , $N(E) = \exp((E - E_0)/T)$, where T is the "nuclear temperature" and E_0 is the energy shift. These two parameters are determined by fitting the cumulative number of available experimental states up to some cut-off energy. The level density parameters for all three residual nuclei involved in CN cross section calculations are listed in Table I. Cumulative number of levels as calculated by the "constant temperature" model using these parameters is shown as solid lines in figure 2.

D. Search procedure

It is well known that search routine does not always converge on optimum solution specially when we are dealing with strongly correlated OMP parameters. In our DOM analysis we performed a global χ^2 optimization combined with a grid search using a χ^2 fit in a limited energy region using a maximum number of two fitting parameters simultaneously. Our search procedure can be divided in four main steps:

1. Search for imaginary $W_v^{emp}(E)$ empirical potential depth using total cross section data between 70 and 150 MeV, neglecting real and imaginary surface contribution. This energy range is selected in order to neglect surface absorptive potential in the first iteration. Once empirical values $W_v^{emp}(E)$ were obtained a fit of the absorptive

volume potential $W_v(E)$ using equation (12) is carried out. In this way volume absorption is fixed, as well as dispersive volume contribution $\Delta V_v(E)$ to the central real potential, which is calculated by integration. The empirical values of the real volume potential depth $V_v^{emp}(E)$ combined with the $\Delta V_v(E)$ are used to obtain a set of empirical points corresponding to $V_{HF}^{emp}(E)$. A typical set of empirical values derived in the above described way can be seen in figure 3, as obtained with the search code COH. Finally the equation (9) is used to obtain the V_0 and α_{HF} parameters that offer a best fit to the empirical real potential data. In the fitting process the strength V_0 was constrained for the DOM predicted first-particle and first-hole states to be centered around the experimental value of the Fermi energy.

2. At each energy for which neutron elastic differential cross section and neutron total cross section data are available from 1 up to 26 MeV, we have conducted a best χ^2 fit by searching on volume real $V_v^{emp}(E)$ and surface imaginary $W_s^{emp}(E)$ empirical potential depths. In the first iteration the corresponding dispersive surface contribution $\Delta V_s(E)$ to the central real potential was calculated by integration from the starting OMP parameters. CN contributions and width fluctuations corrections were considered in all calculation for incident energy below 12 MeV. Once empirical values $W_s^{emp}(E)$ were obtained a fit of the absorptive surface-peaked potential $W_s(E)$ using equation (13) is carried out. Dispersive surface contribution $\Delta V_s(E)$ to the central real potential is re-evaluated by integration. The empirical values of the real volume potential depth $V_v^{emp}(E)$ combined with the $\Delta V_v(E)$ calculated for these energies are used to increase the set of empirical points corresponding to $V_{HF}^{emp}(E)$. The equation (9) is used to refine the fitting of the V_0 and α_{HF} parameters, derived in point (1), using the whole empirical set of potential values obtained in steps (1) and (2). We iterate over steps (1) and (2) until the empirical potential strengths were consistent with our predefined energy functional (see equations (9),(13) and (12)) over the whole energy range
3. After fixing potential strengths, the optimum geometry parameters were searched for, iterating over steps (1) and (2) to redefine the potential strengths corresponding to the optimized geometry parameters
4. Finally a global χ^2 optimization using the whole experimental database was carried out to obtain the minimum in the χ^2 multiparameter surface.

E. The $^{27}Al(n, n)$ DOM analysis

We started our analysis by using non-relativistic formulation to fit the experimental data. Initial values for geometrical parameters were provided by the energy independent geometry deduced by Whisnant *et al* [41] and used by Petler *et al* [36] for phenomenological analysis of the data up to 26 MeV. They found $r_v = 1.18$ fm, $a_v = 0.64$ fm and $r_s = 1.26$ fm, $a_s = 0.58$ fm. Because the general form of the energy dependence of the imaginary potential used in the present model is similar to the $^{27}Al(n, n)$ phenomenological OMP of Lee *et al* [38], we used their volume real and imaginary potential parameters as a starting point for our analysis. We were using symmetric imaginary absorptive potentials according to equations (13) and (12), therefore we adjusted 7 parameters, namely (V_0, α_{HF}), which define the smooth energy dependence of the real volume potential and (A_v, B_v) and (A_s, B_s, C_s) defining the volume and surface absorptive potential respectively. After proper values were obtained by this global minimization the energy independent geometry parameters were also optimized. The derived non-relativistic DOM potential parameters are listed in Table II.

The final σ_T DOM fits using non-relativistic potential are compared to $^{27}Al(n, n)$ data in Fig.4. It should be stressed that experimental total cross section data(except the grayed one) shown in this figure were not used in the DOM parameter search. We can observe that the experimental total cross section at energies above 130 MeV was always underestimated by our nonrelativistic calculations. We can not change the real volume potential depth (or the so called Hartree-Fock potential) without spoiling the fits to the differential cross section. One solution could be to consider an increase of the radius of real part of the OMP. However this approach would obscure our treatment with energy independent geometry. Furthermore, it is theoretically obvious, that relativistic effects and non-locality should show up at this energy regime. Therefore we decided to carry out a full relativistic treatment, including non-local contribution to the absorptive potential, which will be reflected on the dispersive contribution to the real potential.

The starting point in this second stage was the non-relativistic DOM potential. We took into account the non-local contribution to the volume absorptive potential according to equations (15) and (16). Only one additional parameter was included, namely the energy E_a above which the non-local behavior of the volume absorptive potential is considered. In this later χ^2 minimization the total cross section data up to 250 MeV were included into the experimental database. All potential parameters changed because of the sizeable contribution of the non-local absorption for energies above 40 MeV as can be seen from figure 5. In the same figure the total cross section calculated with the

non-relativistic DOM potential is shown for comparison. It is interesting to remark that relativistic correction alone is clearly not enough for the correct description of the total cross section from 130 up to 250 MeV. The final set of parameters of our dispersive relativistic optical model potential is summarized in Table III.

F. Comparison with the experimental cross section in the energy domain $0.1 < E < 250$ MeV

We now compare the experimental cross sections with those calculated from our DOM potentials. The geometrical parameters of the model and the strengths of the various components are specified in Tables II and III. The dispersion relations fully determine the real part of the dispersive contribution once the imaginary part of the mean field is specified.

The $\sigma(\theta)$ relativistic DOM fits are compared to $^{27}\text{Al}(n, n)$ data in figure 6. In general, the fits to $\sigma(\theta)$ are of high quality. Very good agreement between experimental data and calculations is observed in the energy region below 12 MeV, where CN contribution is important. The highest deviation is observed for energies 25-26 MeV located near the diffraction maximum. In this energy region a difficulty was encountered during the fit process evidenced by the fact that a *common* set of surface absorptive potential parameters giving acceptable fits to each type of data (differential and total cross section) could not be found. The fits to $\sigma(\theta)$ indicate smaller values of the imaginary surface potential depth A_s parameter while fits to total cross section point to a values larger by about 2 MeV. Experimental $\sigma(\theta)$ data for energies higher than 26 MeV were not included in the minimization procedure, but our relativistic DOM potential displays an excellent agreement with these data.

The σ_T relativistic DOM fit is compared with the total cross section data and with calculations using phenomenological potentials in figures 7 and 8. It should be stressed that only the Finlay *et al* [32,33] experimental total cross section data, shown as grey circles was used in the DOM parameter search. In figure 7, the total cross section fit is in excellent agreement with the experimental data in the whole energy range from 10 to 250 MeV. The only phenomenological potential which gives a comparable agreement with experimental data up to 200 MeV is the one by Koning and Delaroche [39], being slightly larger than data in the region of the cross section maximum. Madland OMP overestimates the experimental cross section by almost 20 % above 100 MeV. The σ_T relativistic DOM fit is compared to the high resolution total cross section data measured by Ohkubo [71] and Rohr *et al* [72] in figure 8. The total cross section fit using relativistic DOM potential is in good agreement with the averaged experimental data in the whole energy range from 0.1 up to 10 MeV and practically equal to the cross section derived from phenomenological OMP by Petler *et al* [36]. The total cross section calculated by the phenomenological potential of Koning and Delaroche [39] is smaller than the one calculated by the relativistic DOM potential of the present work in the whole energy range from 0.1 up to 10 MeV, but the shape remains quite similar for all compared total cross section calculations. Calculation using relativistic DOM potential, including reorientation effects by considering *Al* as a deformed nucleus ($\beta = 0.4$) with ground state spin equal 2.5 is shown as dashed line in the figure 8. This calculation was carried out without readjusting any potential parameter to see the effect of deformation on the total cross section. Maximum energy in this calculation was equal to the energy of the first excited level to avoid complexity linked to the coupled channel approach. We can see that reorientation effects lead to the reduction of the calculated cross section by 10% from 0.1 up to 0.8 MeV. The small differences between the solid and dashed curves are a measure of the error incurred by the neglect of reorientation effects and nuclear deformation.

Figure 9 shows the comparison between the experimental analyzing power and differential cross section at 7.5-7.6 MeV and the predictions of our relativistic DOM. The agreement is good in view of the fact that these data were not used in our fitting procedure. It can be seen that CN contribution is still quite important at this energy. Polarization measurements at 11 and 14 MeV are compared with DOM calculations in figure 10.

Average volume integral for the real part of the optical potential was determined for the relativistic DOM potential as well as for the available phenomenological potentials and is shown in figure 11. In the same figure the "Hartree-Fock", volume and surface dispersive contributions are shown. The biggest difference between our DOM potential and the phenomenological ones are located below 50 MeV, where surface dispersive contribution reach minimum and then changes the sign, becoming positive. This pure dispersive effect can not be simulated by any variation of the phenomenological OMP parameters. It is interesting that real volume integral above 200 MeV is dominated by the dispersive volume contribution as a result of the non-locality.

Average volume integral for the imaginary part of the optical potential was also calculated. In this case they are big differences between phenomenological potentials and DOM results as can be seen in figure 12. Low energy behaviour is different as was the case for the real volume integral, because the dominance of the dispersive contribution. However high energy region is also quite different. DOM integral increases with energy as a result of the non-locality contribution to the volume absorptive potential. The only phenomenological potential showing similar behaviour is the Madland OMP [37]. His imaginary volume integral goes parallel to the integral calculated using relativistic DOM

potential (not considering a discontinuity caused by two different functional forms employed for reduced radius by Madland; one below 140 MeV, the second above this value). There is a clear connection between this increase of the imaginary volume integral and the saturation of the reaction cross section at energies above 125 MeV as shown in figure 13. This behaviour is consistent with the semiclassical estimation of the reaction cross section. The relativistic DOM potential reaction cross section reaches a near constant value of 0.3 barn. The asymptotical estimate of the reaction cross section is πR^2 equivalent to the reduced radius of 1.03 fm. This value compares well with the averaged reduced radius of 1.1-1.2 fm used for the imaginary potential geometry of the DOM potential. It is interesting to point out that different reaction cross sections will have a direct impact on cross sections available for any statistical model calculations.

IV. CONCLUSIONS

In this work we have presented a dispersive relativistic spherical optical model analysis of neutron scattering up to 250 MeV for ^{27}Al nucleus. The excellent overall agreement obtained between predictions and experimental data would not have been possible without including dispersive terms in the calculations and non-locality effects in the volume absorptive potential. New high precision scattering measurements for the aluminium above 30 MeV are necessary to establish our analysis on firmer grounds and confirm our present results.

ACKNOWLEDGMENTS

This work was supported by Junta de Andalucía and the spanish CICYT under contract PB1998-1111 and by the European Union under contract FIKW-CT-2000-00107. One of the authors (R.C.) acknowledges support from the Ministerio de Educación, Deportes y Cultura de España, Secretaría de Estado de Educación y Universidades.

-
- [1] C. Mahaux and H. Ngo. *Nucl Phys.* **A431**, 486, (1984).
 - [2] C. Mahaux and R. Sartor. *Nucl Phys.* **A468**, 193, (1987).
 - [3] C.H. Johnson, D.J. Horen, and C. Mahaux. *Phys. Rev. C* **36**, 2252, (1987).
 - [4] C. Mahaux and R. Sartor. *Nucl. Phys.* **A528**, 253, (1991).
 - [5] J.W. Negele and E. Vogt, editors. *Advances in Nuclear Physics.* (Plenum, New York, 1991), 1991.
 - [6] M.A. Nagarajan, C. Mahaux, and G.R. Satchler. *Phys. Rev. Lett.* **54**, 1136, (1985).
 - [7] C. Mahaux, H. Ngo, and G.R. Satchler. *Nucl Phys.* **A449**, 354, (1986).
 - [8] M. Lozano. *Phys. Rev. C* **36**, 452, (1987).
 - [9] Y. Wang, C.C. Foster, E.J. Stephenson, L. Yuan, and J. Rapaport. *Phys. Rev. C* **45**, 2891, (1992).
 - [10] C.H. Dasso, R.J. Liotta, and M. Lozano. *Phys. Rev. C* **54**,, (1996).
 - [11] C. Mahaux and R. Sartor. *Nucl. Phys.* **A484**, 205, (1988).
 - [12] C. Mahaux and R. Sartor. *Nucl. Phys.* **A493**, 157, (1989).
 - [13] C.H. Johnson and C. Mahaux. *Phys. Rev. C* **38**, 2589, (1988).
 - [14] W. Tornow, Z.P. Chen, and J.P. Delaroche. *Phys. Rev. C* **42**, 693, (1990).
 - [15] J.P. Delaroche, Y. Wang, and J. Rapaport. *Phys. Rev. C* **39**, 391, (1989).
 - [16] S. Chiba, P.T. Guenter, A.B. Smith, M. Sugimoto, and R.D. Lawson. *Phys. Rev. C* **45**, 1260, (1992).
 - [17] Y. Wang, C.C. Foster, R.D. Polak, J. Rapaport, and E.J. Stephenson. *Phys. Rev. C* **47**, 2677, (1993).
 - [18] C. Mahaux and R. Sartor. *Nucl. Phys.* **A568**, 1, (1994).
 - [19] R.W. Finlay, J. Wierzbicki, R.K. Das, and F.S. Dietrich. *Phys. Rev. C* **39**, 804, (1989).
 - [20] G.J. Weisel, W. Tornow, C.R. Howell, P.D. Felsher, M. AlOhal, M.L. Roberts, R.K. Das, R.L. Walter, and G. Mertens. *Phys. Rev. C* **54**, 2410, (1996).
 - [21] X. X. Zhang, Z. Chen, Y. Chen, J. Yuan, G. Tang, G. Zhang, J. Chen, Yu.M. Gledenov, G. Kluukhenkhuu, and M. Sedysheva. *Phys. Rev. C* **61**, 054607, (2000).
 - [22] R.D. Lawson, P.T. Guenther, and A.B. Smith. *Nucl. Phys.* **A493**, 267, (1989).
 - [23] C.H. Johnson, R.F. Carlton, and R.R. Winters. *Phys. Rev. C* **39**, 415, (1989).
 - [24] C. Mahaux and R. Sartor. *Phys. Rev. C* **36**, 1777, (1987).
 - [25] A.B. Smith, P.T. Guenther, and R.D. Lawson. *Nucl. Phys.* **A455**, 344, (1986).
 - [26] S. Chiba, P.T. Guenter, R.D. Lawson, and A.B. Smith. *Phys. Rev. C* **42**, 2487, (1990).

- [27] R.K. Das and R.W. Finlay. *Phys. Rev. C* **42**, 1013, (1990).
- [28] G.J. Weisel and R.L. Walter. *Phys. Rev. C* **59**, 1189, (1999).
- [29] M.M. Nagadi, J.P. Delaroche, C.R. Howell, W. Tornow, and R.L. Walter. The dispersive optical model for $n + {}^{27}\text{Al}$. Technical report, TUNL-XXIX, p.87, Triangle University Nuclear Lab., 1990.
- [30] E.A. Romanovsky, H.A. Hussein, and R.I. Bogdanov. *Izv.Akad.Nauk SSSR, Ser.Fiz.* **53**, 156, (1989).
- [31] E.A. Romanovsky and T.I. Spasskaya. *Izv.Akad.Nauk SSSR, Ser.Fiz.* **59**, 136, (1995).
- [32] R.W. Finlay, F. Fink, W. Abfalterer, P. Lisowski, G.L. Morgan, and R.C. Haight. In *Proceedings of the Nuclear Data for Science and Tecnology Conference, Julich, 1991, ed. by S. M. Qaim (Springer-Verlag, Berlin, Hildelberg, New York, 1992), p.720*.
- [33] R.W. Finlay, W. Abfalterer, F. Fink, E. Montei, T. Adami, P. Lisowski, G.L. Morgan, and R.C. Haight. *Phys. Rev. C* **47**, 237, (1993).
- [34] A.J. Koning, J.P. Delaroche, and O. Bersillon. *Nucl.Instrum.Method.Phys.Res.* **A414**, 49, (1998).
- [35] M. B. Chadwick *et al.* *Nucl. Sc. Eng.* **1331**, 293, (1999).
- [36] J.S. Petler, M.S. Islam, R.W. Finlay, and F.S. Dietrich. *Phys. Rev. C* **32**, 673, (1985).
- [37] D.G. Madland. Recent results in the development of a global medium-energy nucleon-nucleus optical-model potential. In *Proceedings of the Specialists' Meeting on Preequilibrium Nuclear Reactions. Semmering, Austria, 1988, edited by B. Strohmaier, Nuclear Energy Agency Nuclear Data Committee Report No- NEANDC-245 'U', Paris 1988, p.103*.
- [38] Y.O. Lee, J. Chang, T. Fukahori, and S. Chiba. *J. Nucl. Sci. and Tech. (Tokyo)* **36**, 1125, (1999).
- [39] A. Koning and J.P. Delaroche. *unpublished (submitted to Phys. Rev. C, (july 2001)*.
- [40] A. Nadasen, P. Schwandt, W.W. Jacobs, A.D. Bacher, P.T. Debevec, M.D. Kaitchuck, and J.T. Meek. *Phys. Rev. C* **23**, 1023, (1981).
- [41] C.S. Whisnant, J.H. Dave, and C.R. Gould. *Phys. Rev. C* **30**, 1435, (1984).
- [42] R. Lipperheide. *Z. Phys.* **202**, 58, (1967).
- [43] G.E. Brown and M. Rho. *Nucl Phys.* **A372**, 397.
- [44] *Handbook for Calculations of nuclear reaction data: Reference Input Parameter Library.* (International Energy Agency, Vienna, Austria, 1998).
- [45] C. Mahaux and R. Sartor. *Nucl Phys.* **A458**, 25, (1986).
- [46] J.M. van der Kam, G.J. Weisel, and W. Tornow. *J. Phys. G:Nucl.Part.Phys.* **26**, 1787, (2000).
- [47] J. Raynal. Optical model and coupled-channels calculations in nuclear physics. In *Computing as a language of physics. ICTP International Seminar Course, Trieste, Italy, Aug.2-10, 1971 (IAEA, 1972), page 281*.
- [48] J. Raynal. Program ECIS95.
- [49] T. Kawano. Program COH.
- [50] R. Capote, A. Molina, and J.M. Quesada. *J. Phys. G:Nucl.Part.Phys.* **27**, B15, (2001).
- [51] J.H. Towle and W.B. Gilboy. *Nucl. Phys.* **39**, 300, (1962).
- [52] S. Tanaka, K. Tsukada, M. Maruyama, and Y. Tomita. In *Nuclear Data for Reactors Conference, Helsinki, 1970*.
- [53] W.E. Kinney and F.G. Perey. Technical report, ORNL-4516, Oak Ridge National Laboratory, 1976.
- [54] G. Dagge, W. Grumm, J.W. Hammer, K.-W. Hoffmann, and G. Schreder. *Phys. Rev. C* **39**, 1768, (1989).
- [55] D.E. Velkley, D.W. Glasgow, M.T. Brandenberger, J.D. and Mc Ellistrem, J.C. Manthuruthil, and C.P. Poirier. *Phys. Rev. C* **9**, 2181, (1974).
- [56] G. Boerker, R. Boettger, H.J. Brede, H. Klein, W. Mannhart, and R.L Siebert. In *Proceedings of the International Conference on Nuclear Data For Science and Technology, Mito, Japan, 1988*.
- [57] A. Bratenahl, S. Fernbach, R.H. Hildebrand, C.E. Leith, and B.J. Moyer. *Phys. Rev.* **77**, 597, (1950).
- [58] G.L. Salmon. *Nucl. Phys.* **21**, 15, (1960).
- [59] C.P. Van Zyl, R.G.P. Voss, and R. Wilson. *Phylos. Mag.* **1**, 1003, (1956).
- [60] Ph. Martin and R.L. Walter. *Phys. Rev. C* **34**, 384, (1986).
- [61] J. de Juren and B.J. Moyer. *Phys. Rev.* **81**, 919, (1951).
- [62] A.E. Taylor and E. Wood. Neutron total cross section between 30 and 153 MeV. *Phylos. Mag.* **44**, 95, (1953).
- [63] P.H. Bowen, J.P. Scanlon, G.H. Stafford, J.J. Thresher, and P.E. Hodgson. *Nucl. Phys.* **22**, 640, (1961).
- [64] D.F. Measday and J.N. Palmieri. *Nucl. Phys.* **85**, 129, (1966).
- [65] R.J. Schneider and A.M. Cormack. *Nucl. Phys.* **119**, 197, (1968).
- [66] S. Cierjaks, P. Forti, D. Kopsch, L. Kropp, J. Nebe, and H. Unseld. Technical report, Kernforschungszentrum Karlsruhe Report, Nos. KFK-1000, EUR-3963E and EANDC(E)-111, 1968.
- [67] Jr. Foster, D.G. and D.W. Glasgow. *Phys. Rev. C* **3**, 576, (1971).
- [68] F.G. Perey, T.A. Love, and W.E. Kinney. A test of neutron total cross-section evaluations from 0.2 to 20 MeV for C, O, Al, Si, Ca and SiO_2 . Technical report, ORNL-4823, Oak Ridge National Laboratory, 1972.
- [69] D.C. Larson, J.A. Harvey, and N.W. Hill. Measurement of neutron total cross sections at ORELA to 80 MeV. Technical report, ORNL-5787, p.174, Oak Ridge National Laboratory, 1981.
- [70] J. Franz, H.P. Grotz, L. Lehmann, E. Roessle, H. Schmitt, and Schmitts L. *Nucl. Phys.* **A490**, 667, (1988).
- [71] M. Ohkubo. In *Proceedings of the International Conference on Nuclear Data for Basic and Applied Science, Santa Fe, N.M., 1985*.

- [72] G. Rohr, R. Shelley, C. Nazareth, and M. Moxon. In *Conference on Nuclear Data for Science and Technology, 1994, Gatlinburg, Tenn., USA*.
- [73] R.B. Schwartz, R.A. Schrack, and H.T. Heaton. Technical report, NBS-MONO-138, National Bureau of Standards, 1974.
- [74] W. Hauser and H. Feshbach. *Phys. Rev.* **87** 366, (1952).
- [75] P.A. Moldauer. *Nucl. Phys.* **A344**, 185, (1980).
- [76] F.G. Perey. *Phys. Rev.* **131**, 745, (1963).
- [77] E.D. Arthur and P.G. Young. Evaluation of neutron cross sections to 40 MeV for $^{54,56}\text{Fe}$. In *Proceedings of the Symposium on Neutron Cross Sections from 10 to 50 MeV. Brookhaven National Laboratory, Upton, N.Y. edited by M.R. Bhat and S. Pearlstein, Brookhaven National Laboratory Report No. BNL-NCS-51245, 1980, Vol-II, p. 731*.
- [78] O.F. Lemos. Technical report, Orsay, Series A No. 136, 1976.
- [79] A. Gilbert and A.G.W. Cameron. *Can. J. Phys.* **43**, 1446, (1965).
- [80] R.C. Harper and W.L. Alford. *J. Phys. G: Nucl. Phys.* **8**, 153, (1982).

TABLE I. Constant temperature level density parameters for residual nuclei in $n + {}^{27}\text{Al}$ reaction

| Residual Nucleus | E_{cut} [MeV] | T [MeV] | E_0 [MeV] |
|--------------------|-----------------|-----------|-------------|
| ${}^{27}\text{Al}$ | 11.2 | 2.071 | -0.678 |
| ${}^{24}\text{Na}$ | 5.2 | 1.875 | -2.046 |
| ${}^{27}\text{Mg}$ | 6.0 | 2.113 | -1.2157 |

 TABLE II. Optical model parameters for non-relativistic dispersive potential for $n + {}^{27}\text{Al}$ reaction up to 150 MeV.

| Parameter(Unit) | Value |
|-------------------------------------|---------|
| V_0 (MeV) | 52.24 |
| α_{HF} (MeV^{-1}) | 0.0071 |
| A_v (MeV) | 12.5 |
| B_v (MeV) | 58.8 |
| r_v (fm) | 1.20 |
| a_v (fm) | 0.65 |
| A_s (MeV) | 12.6 |
| B_s (MeV) | 3.25 |
| C_s (MeV^{-1}) | 0.0395 |
| r_s (fm) | 1.11 |
| a_s (fm) | 0.64 |
| E_F (MeV) | -10.392 |
| E_p (MeV) | -5.66 |

 TABLE III. Optical model parameters for relativistic dispersive potential for $n + {}^{27}\text{Al}$ reaction up to 250 MeV.

| Parameter(Unit) | Value |
|-------------------------------------|---------|
| V_0 (MeV) | 54 |
| α_{HF} (MeV^{-1}) | 0.0087 |
| A_v (MeV) | 7 |
| B_v (MeV) | 65 |
| r_v (fm) | 1.20 |
| a_v (fm) | 0.63 |
| A_s (MeV) | 12.5 |
| B_s (MeV) | 5 |
| C_s (MeV^{-1}) | 0.034 |
| r_s (fm) | 1.11 |
| a_s (fm) | 0.64 |
| E_F (MeV) | -10.392 |
| E_p (MeV) | -5.66 |

FIG. 1. Dependence upon energy of the dispersive volume contribution of the real central potential of the $n+^{27}\text{Al}$ mean field. The dotted curve corresponds to equation (10), in which it is assumed that the imaginary part is symmetric about the Fermi energy. The thick solid curves correspond to the asymmetric model, considering non-local behaviour of the imaginary volume absorption above certain energy E_a following equations (15) and (16). Thin dashed line corresponds to the Fermi energy.

FIG. 2. Cumulative number of levels as a function of the excitation energy for the three residual nuclei considered in the CN cross section calculations. The discrete level data are from the RIPL [44] and are well represented by the "constant temperature" level density formula of Ref. [79] using parameters from Table I. Cut-off energy is indicated by the vertical dashed line. Above the cut-off energy the "constant temperature" level density formula was used

FIG. 3. Empirical real volume (solid circles) and imaginary volume potential depth (empty circles) of the OMP for $n+^{27}\text{Al}$ as determined from individual best χ^2 fit searches using σ_{tot} data in the interval $70 < E < 150$ MeV after the first iteration. (Upper panel) The solid line for the Hartree-Fock potential is the functional representation defined in equation (9). The dashed line denotes the starting guess values calculated using Lee *et al* OMP [38]. The crosses represent the empirical values of the Hartree-Fock type potential obtained after the dispersive contribution coming from the volume imaginary part of the OMP was subtracted from the real volume empirical values. (Lower panel) The solid line for the absorptive potential is the functional representation defined in equation (12). The dashed line denotes the starting guess values calculated using Lee *et al* OMP [38].

FIG. 4. Energy dependence of the $n+^{27}\text{Al}$ total cross section from 10 up to 150 MeV. The curve has been calculated using the non-relativistic (solid line) DOM potential of the present work. Grey circles correspond to Finlay *et al* [32,33] experimental data used in the fitting procedure. The diamonds, crosses and triangles are obtained from the measurements by Tayloret *al* [62], Measdayet *al* [64] and Schneideret *al* [65]

FIG. 5. Relativistic and nonlocality contribution to the total cross section. The total cross section curves have been calculated using the relativistic(solid line) and non-relativistic(dotted line) DOM potentials of the present work. The dashed line denotes relativistic DOM potential results without non-locality correction.

FIG. 6. Comparison between the neutron elastic differential cross section experimental data and our DOM calculations(solid line). CN contributions has been added to the direct reaction predictions for incident energies up to 12 MeV. The $\sigma(\theta)$ data were obtained from Towle and Gilboy [51] at 1,2,3 and 4 MeV; Tanaka *et al* [52] at 4.8,6,7 and 8 MeV; Kinney and Perey [53] at 5.4, 6.4,7.5 and 8.6 MeV; Dagge *et al* [54] at 7.62 MeV; Velkley *et al* [55] at 9 MeV; Boerker *et al* [56] at 10.2 MeV; Whisnant *et al* [41] at 11,14 and 17 MeV and Petler *et al* [36] at 18,20,22,25 and 26 MeV. It should be noted that data above 26 MeV was not used in the fitting process. Neutron incident energy is quoted above each calculated curve.

FIG. 7. Energy dependence of the $n+^{27}\text{Al}$ total cross section above 10 MeV. The curves have been calculated using the relativistic(solid line) DOM potential of the present work. The dotted, dotted-dashed and dashed lines have been obtained from the phenomenological OMP by Madland [37], Leeet *al* [38] and Koning and Delaroche [39] respectively in their range of validity. Grey circles correspond to Finlay *et al* [32,33] experimental data used in the fitting procedure. The diamonds, crosses, triangles, empty circles and solid squares have been obtained from the measurements by Tayloret *al* [62], Measdayet *al* [64], Schneideret *al* [65], Franzet *al* [70] and Juren et *al* [61]

FIG. 8. Low energy dependence of the $n+^{27}\text{Al}$ total cross section from 0.1 up to 10 MeV. The curves have been calculated using the relativistic DOM potential without(solid line) and with(dashed line) reorientation effects. The circles, triangles up and triangles down have been obtained from the phenomenological OMP by Harperet *al* [80], Petleret *al* [36] and Koning and Delarocheet *al* [39]. The high resolution experimental data have been obtained from the measurements by Ohkubo [71] and Rohret *al* [72]

FIG. 9. The CN corrected $\sigma(\theta)$ and $A_y(\theta)$ data (solid line) at $E_n = 7.62$ MeV. Experimental data was taken from Dagge *et al* [54] and Kinney and Perey [53]. Dashed line is denoted the uncorrected for CN contribution polarization and cross section data.

FIG. 10. The $A_y(\theta)$ data (solid line) at $E_n=14$ and 17 MeV. Experimental data was taken from Martin and Walter [60].

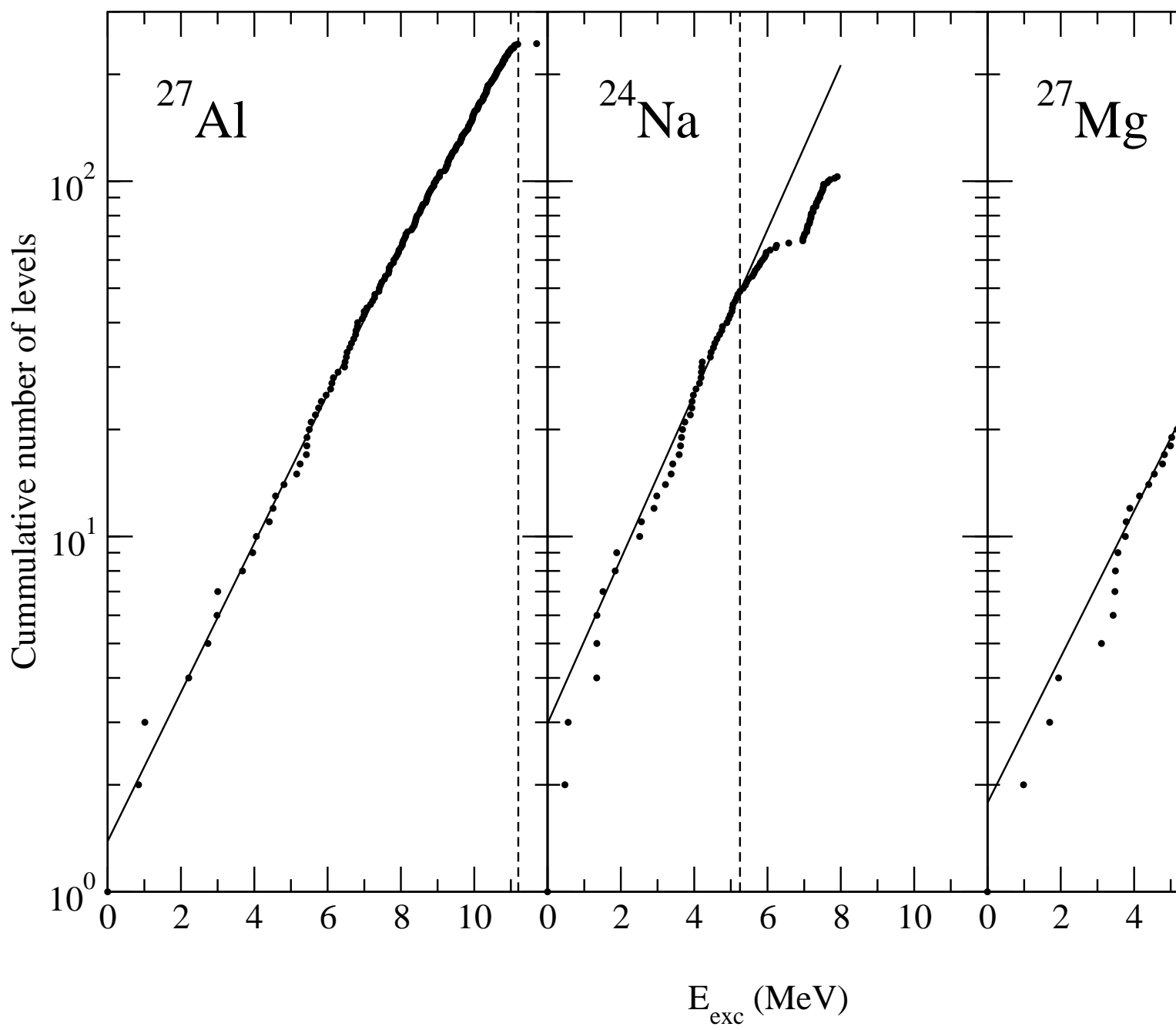
FIG. 11. Energy dependence of the volume integrals per nucleon of the Hartree-Fock(dot-dashed line), volume(dotted line) and surface(dashed line) dispersive components of the real part of the $n + {}^{27}\text{Al}$ mean field. The thick solid curve represents the sum of all contributions. Nonlocality was considered in the volume imaginary potential. The solid squares, solid triangles and empty circles connected by lines have been obtained from the phenomenological OMP by Madland [37], Lee *et al* [38] and Koning and Delaroche [39] respectively.

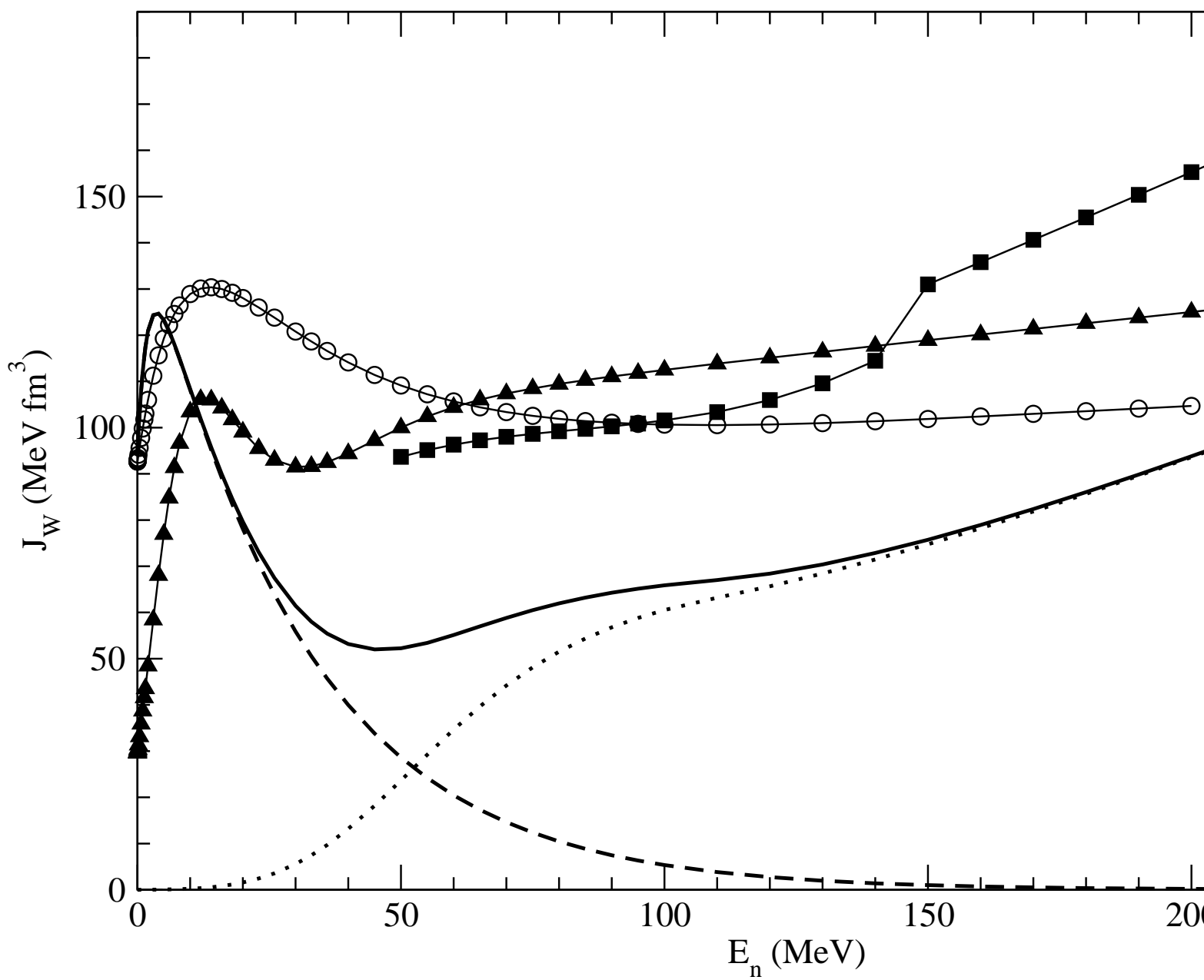
FIG. 12. Energy dependence of the volume integrals per nucleon of the volume (dotted line) and surface-peaked(dashed line) components of the imaginary part of the $n + {}^{27}\text{Al}$ mean field. The solid curve represents the sum of all contributions. Nonlocality was considered in the volume imaginary potential. The solid squares, solid triangles and empty circles connected by lines have been obtained from the phenomenological OMP by Madland [37], Lee *et al* [38] and Koning and Delaroche [39] respectively.

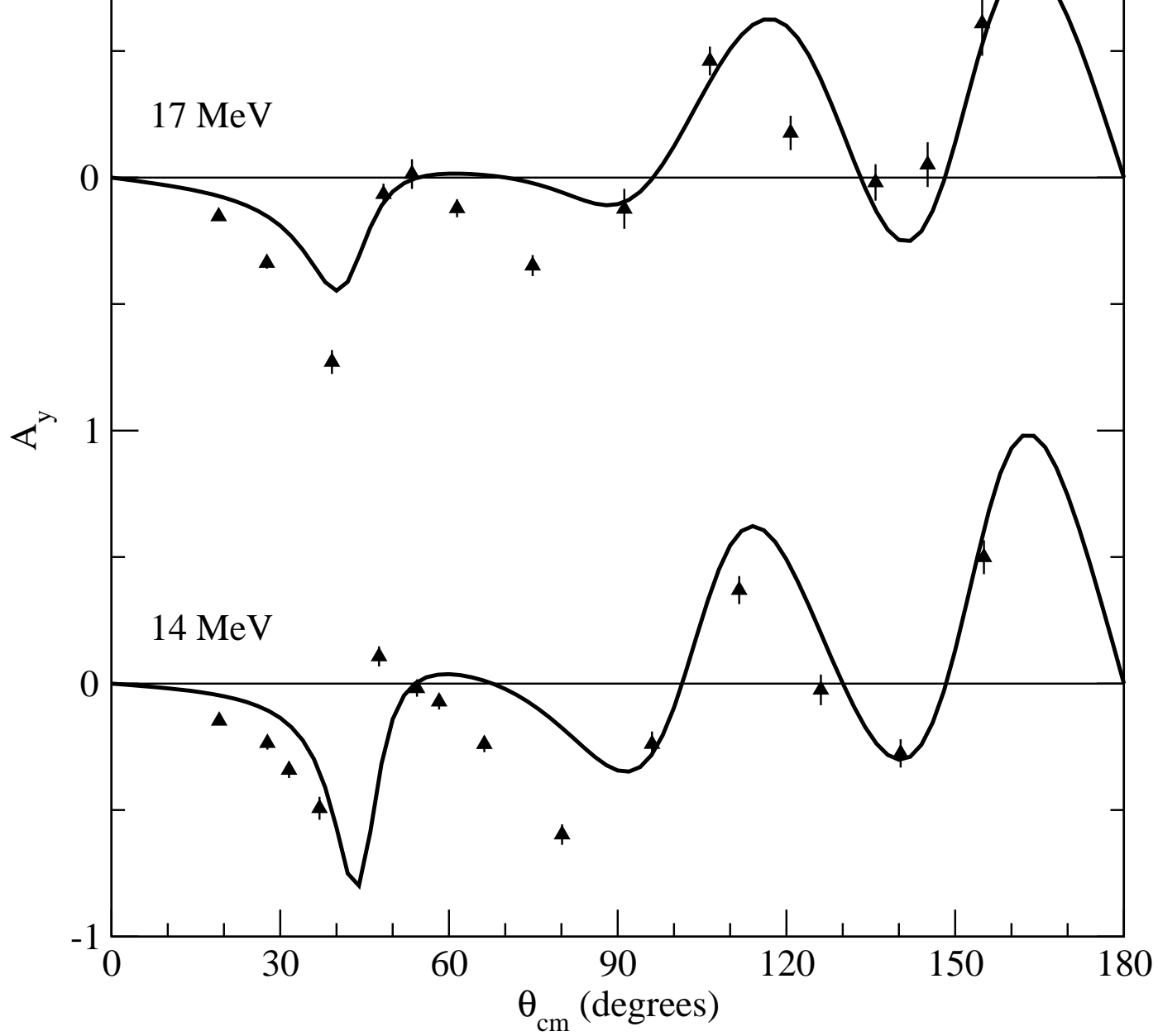
FIG. 13. Energy dependence of the $n + {}^{27}\text{Al}$ reaction cross section from 0.1 up to 250 MeV. The thick solid curve has been calculated using the relativistic DOM potential of the present work. The solid squares, solid triangles and empty circles connected by lines have been obtained from the phenomenological OMP by Madland [37], Lee *et al* [38] and Koning and Delaroche [39] respectively in their range of validity.

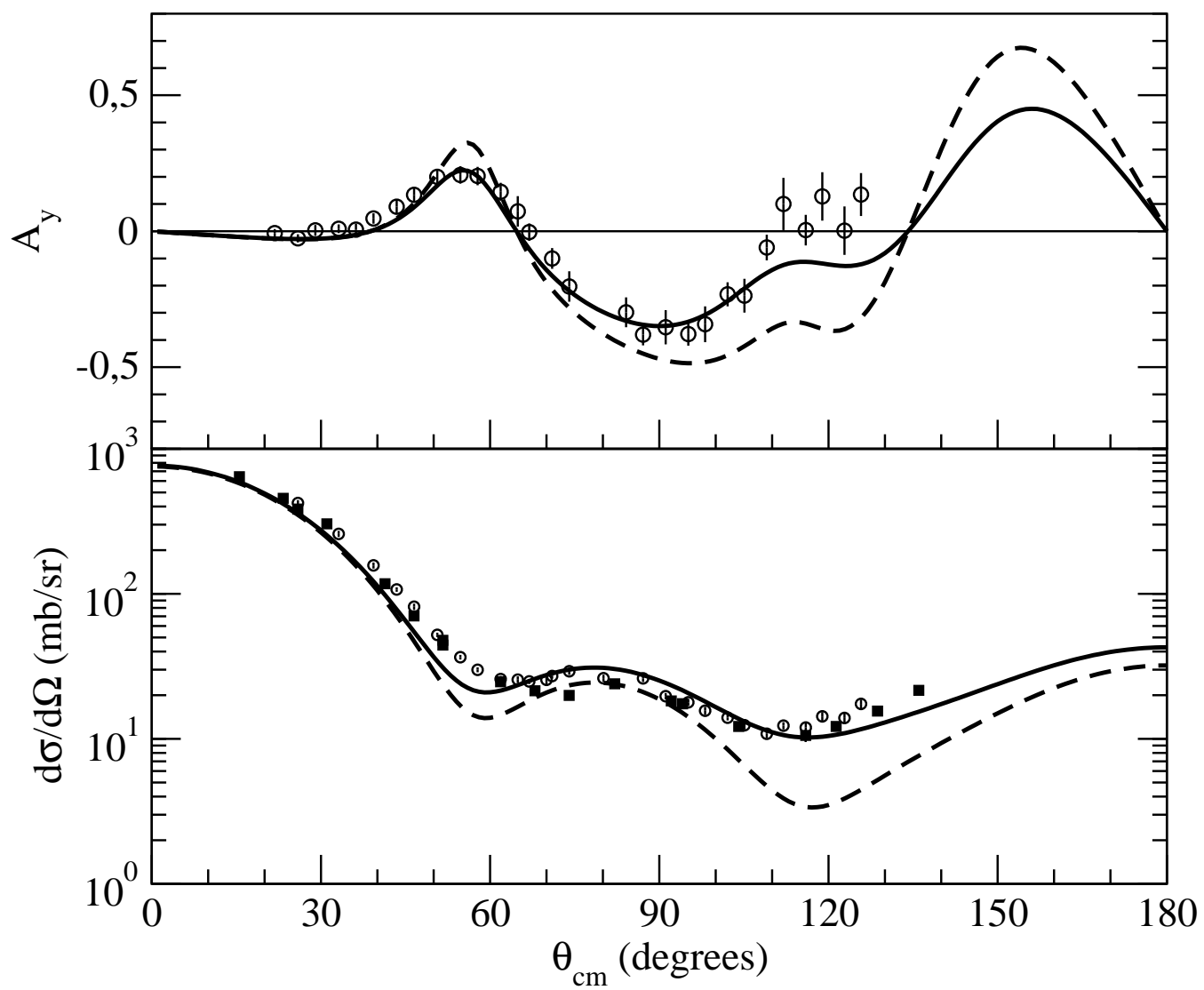
This figure "FIG_ANG_DISTR.JPG" is available in "JPG" format from:

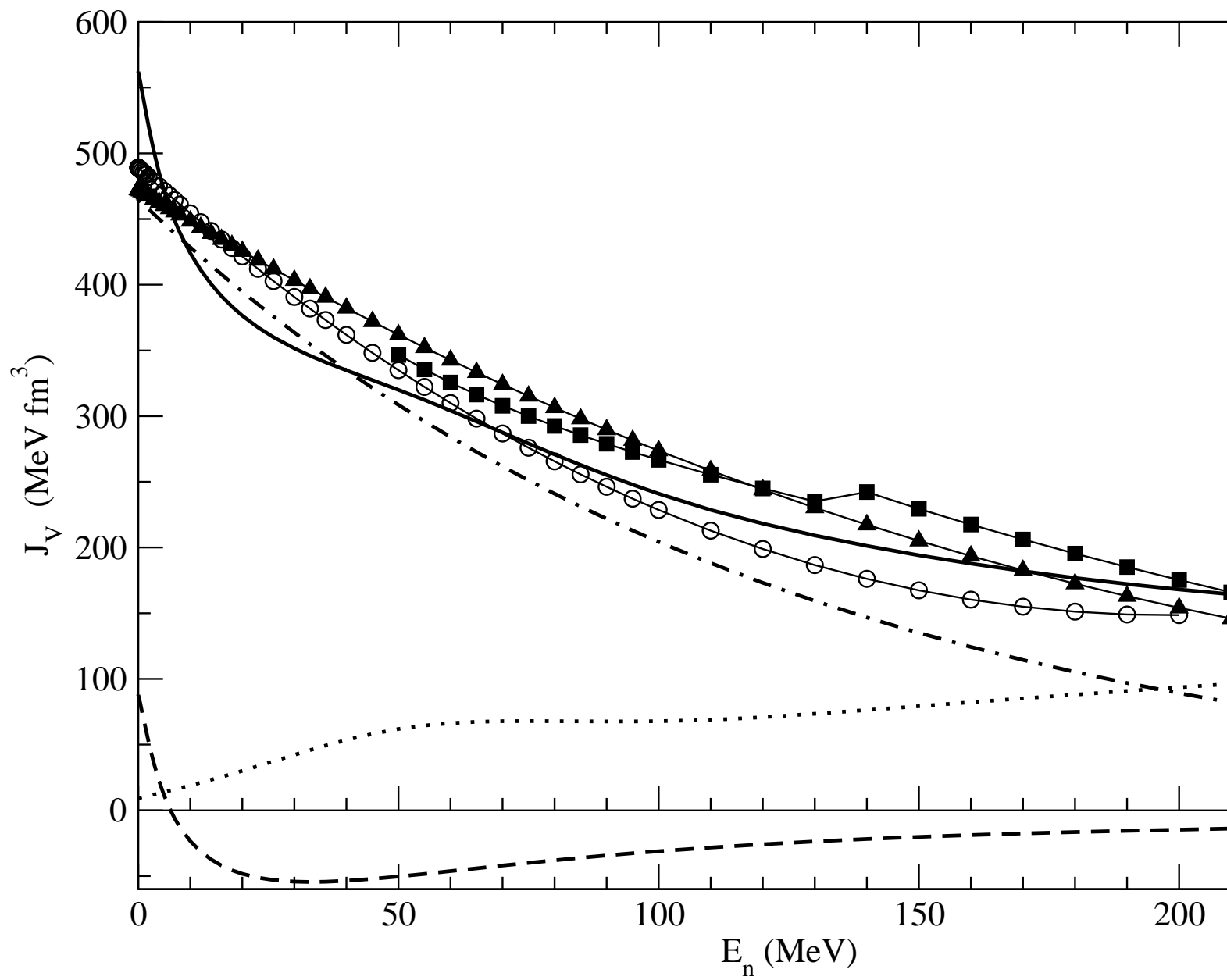
<http://arxiv.org/ps/nucl-th/0111048v1>

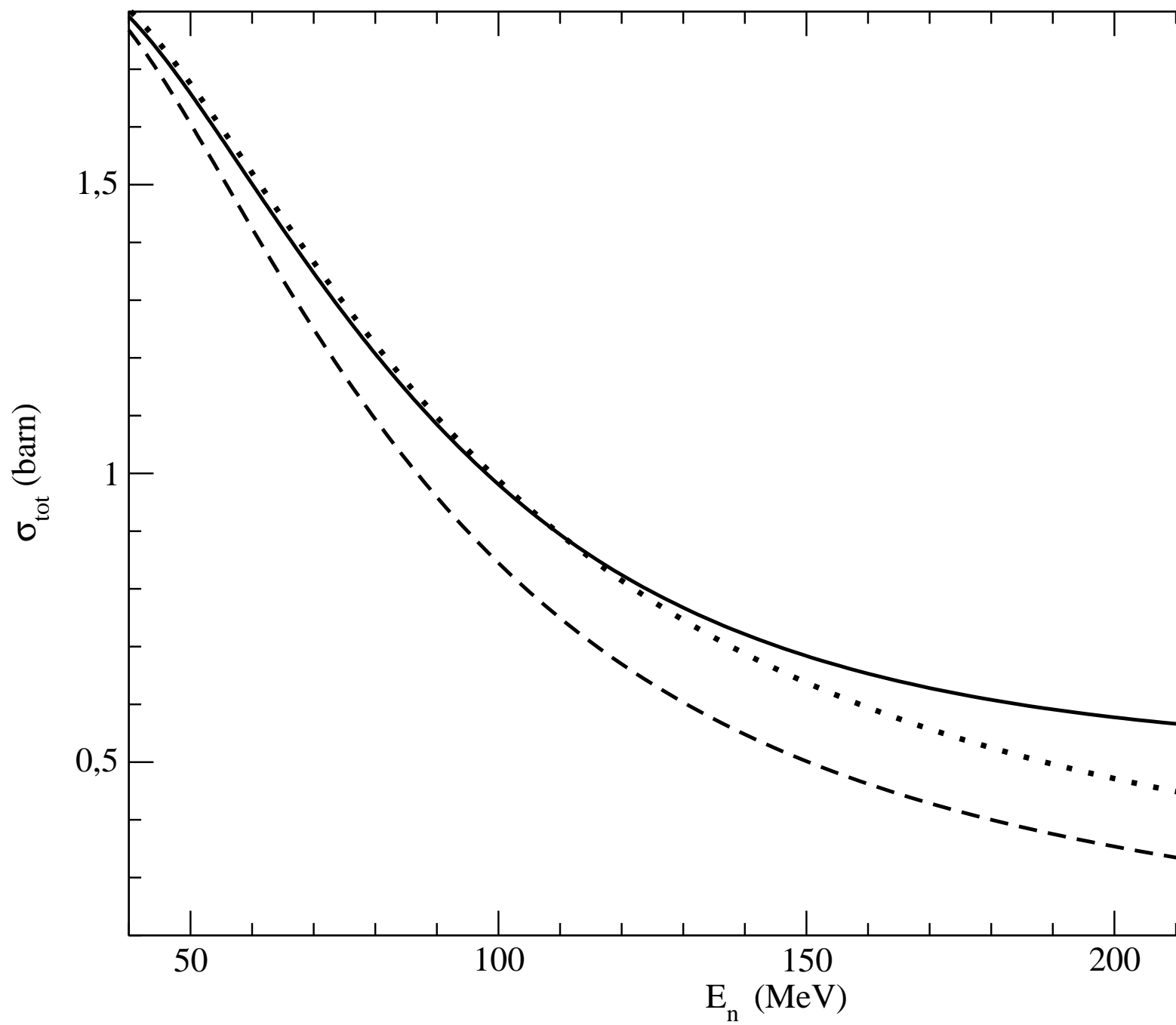


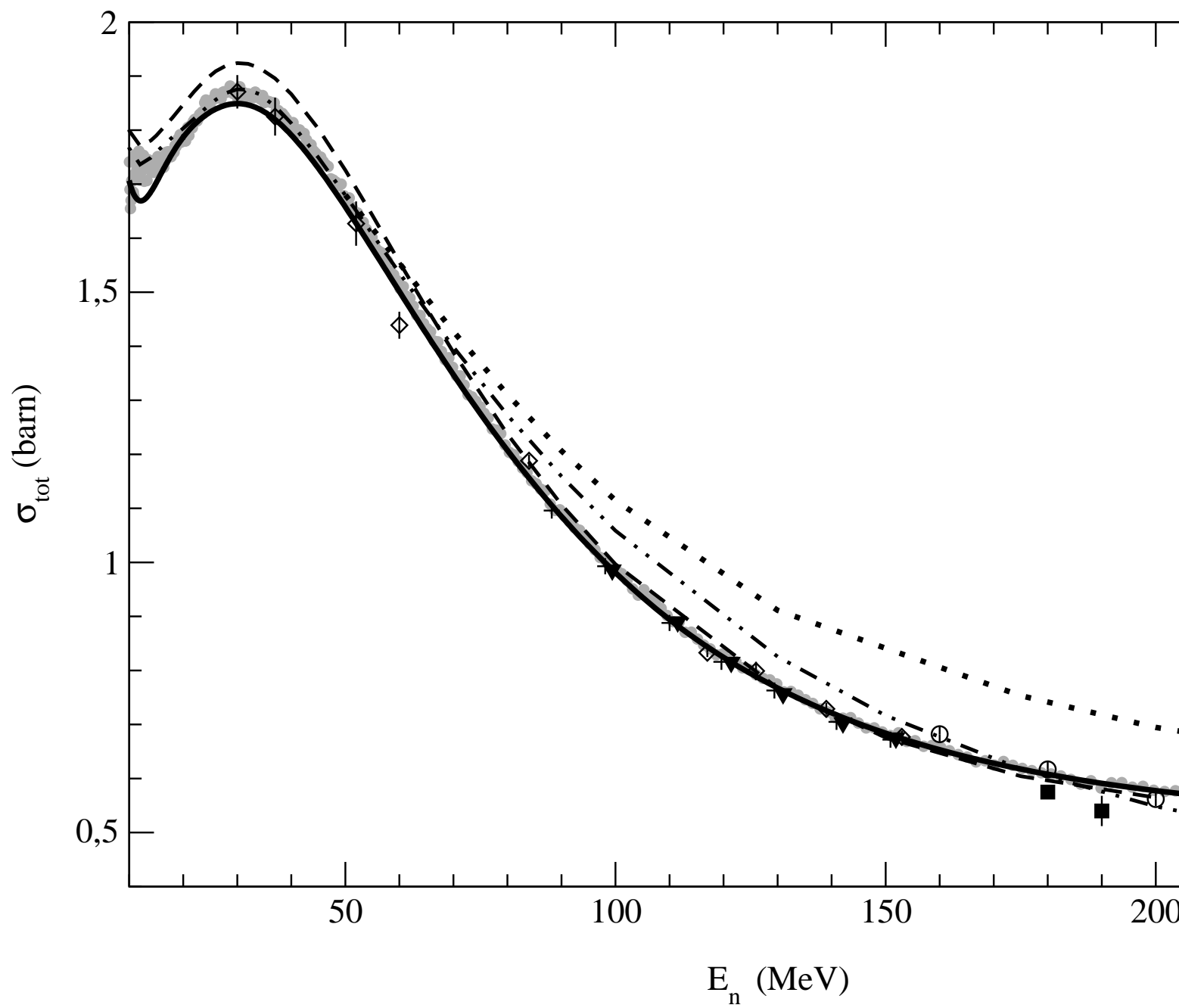


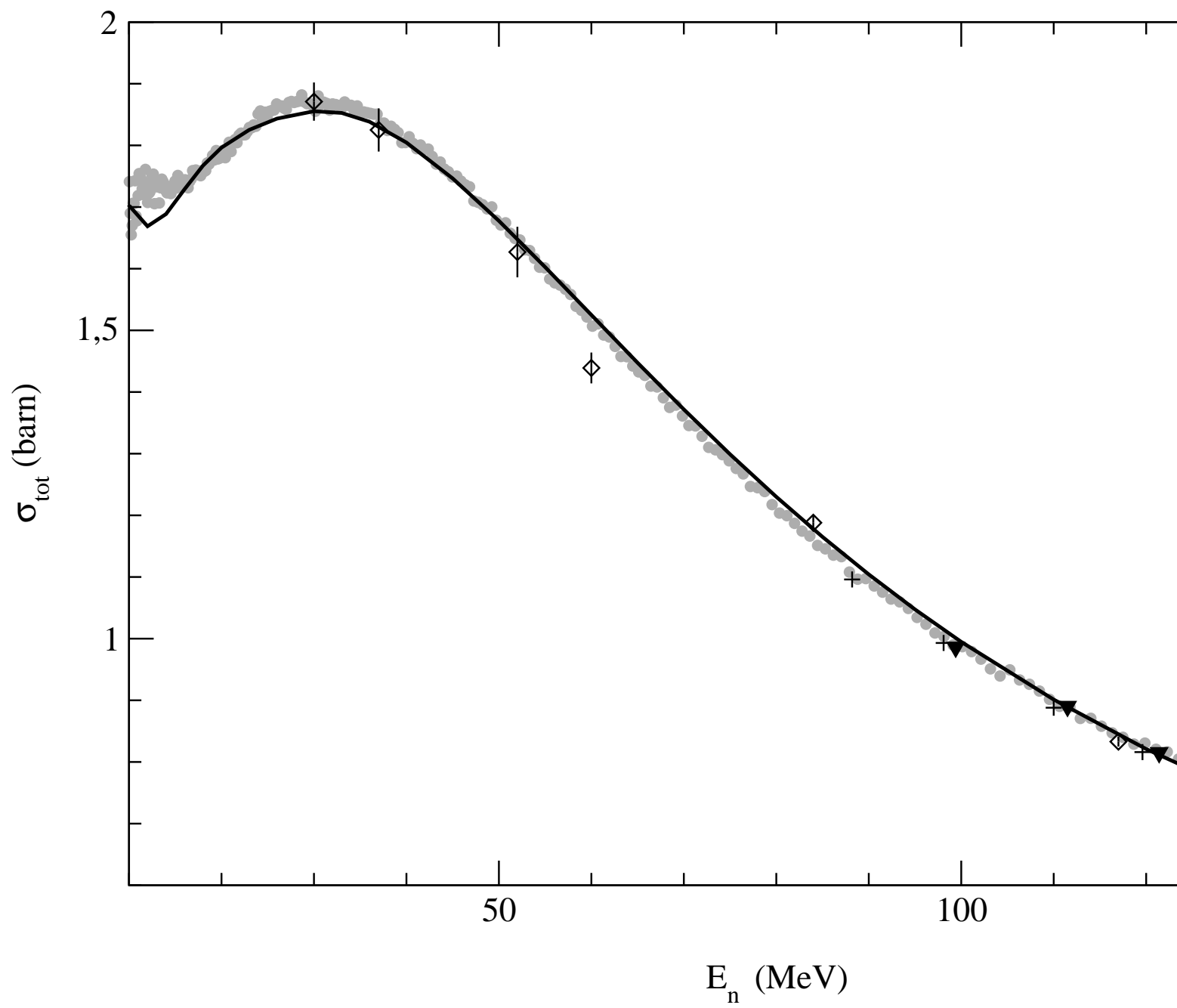












This figure "FIG_SIGMA_LOW_E.JPG" is available in "JPG" format from:

<http://arxiv.org/ps/nucl-th/0111048v1>

